

Gravitational Waves from Neutrino Emission Asymmetries in Core-collapse Supernovae

David Vartanyan¹ and Adam Burrows² Department of Physics and Astronomy, University of California, Berkeley, CA 94720A, USA; dvartany@berkeley.edu

Department of Astrophysical Sciences, Princeton, NJ 08544, USA

Received 2020 July 11; revised 2020 August 14; accepted 2020 August 14; published 2020 September 28

Abstract

We present a broadband spectrum of gravitational waves (GWs) from core-collapse supernovae (CCSNe) sourced by neutrino emission asymmetries for a series of full 3D simulations. The associated GW strain probes the long-term secular evolution of CCSNe and small-scale turbulent activity and provides insight into the geometry of the explosion. For nonexploding models, both the neutrino luminosity and the neutrino gravitational waveform will encode information about the spiral SASI. The neutrino memory will be detectable for a wide range of progenitor masses for a galactic event. Our results can be used to guide near-future decihertz and long-baseline GW detection programs, including aLIGO, the Einstein Telescope, and DECIGO.

Unified Astronomy Thesaurus concepts: Gravitational waves (678); Core-collapse supernovae (304); Supernova neutrinos (1666)

1. Introduction

Core-collapse supernova (CCSNe) explosions are dynamical events involving extreme astrophysical conditions, with the central core reaching super-nuclear densities and temperatures of hundreds of billions kelvin. The relevant timescales in CCSNe range from submilliseconds to seconds, the former associated with the dynamical bounce, rotation, and convective motions and the latter due to secular evolution of the late-time neutrino emissions and explosion debris. No viable CCSNe explosion is spherical (Radice et al. 2017; Burrows et al. 2019, 2020; Müller 2019a; Nagakura et al. 2019; Vartanyan et al. 2019a; with the possible exception of low-mass $\leq 9.5 M_{\odot}$ progenitors which have very steep density profiles and weakly bound mantles, see, e.g., Radice et al. 2017). In general, multidimensional effects are critical to both modeling a successful explosion itself, and parameterized turbulence in spherically symmetric 1D models (Mabanta et al. 2019; Couch et al. 2020) is less than adequate. Due to time-changing quadrupolar motions, CCSNe are classic sources of gravitational waves (GWs), with most of the gravitational-wave energy ($\sim 10^{-8} M_{\odot} c^2$, where M_{\odot} indicates a solar mass) coming out at hundreds to thousands of hertz. A major discriminating spectral signature is the g-mode/f-mode of fundamental oscillation of the proto-neutron star (PNS) that evolves to higher frequencies as the core deleptonizes and cools on its way to the cold, catalyzed neutron star state. This mode is excited by asymmetrically infalling plumes of matter that hammer the PNS in the first seconds of core-collapse and explosion and is an important asteroseismological measure of core structure and early evolution. The modern theory of this dominant GW component of CCSNe is summarized in Morozova et al. (2018) and in Radice et al. (2019), and in references therein (see also Sotani et al. 2017; Torres-Forné et al. 2018, 2019; Mezzacappa et al. 2020).

However, the low-frequency component below ~ 10 Hz, not so easily measured even by next generation ground-based platforms, bears the stamp of important secular motions. The first is due to ejecta motions themselves. The explosions are generically asymmetrical, with matter ejection and core recoil kicks on timescales of 0.1 to a few seconds (Burrows &

Hayes 1996; Murphy et al. 2009; Holgado & Ricker 2019). Interestingly, the metric perturbations do not necessarily return to zero, and the metric is permanently shifted. This is akin to the classical "memory" effect (Christodoulou 1991; Thorne 1992), but is due to asymmetrical matter ejection. The associated frequencies are $\sim 0.1-10\,\mathrm{Hz}$. It is thought that pulsars are born with kicks due either to asymmetrical ejecta or to asymmetrical neutrino emission and the associated momentum recoils. Though momentum asymmetries are dipolar phenomena, there is always an associated quadrupolar component (Vartanyan et al. 2019a).

Along with the longer-term secular matter component at low frequencies, intriguingly there is a similar contribution due to asymmetrical neutrino emissions (Epstein 1978; Turner 1978; Braginskii & Thorne 1987; Burrows & Hayes 1996; Müller & Janka 1997; Kotake et al. 2006, 2009a, 2011; Kotake 2010; Müller et al. 2012, 2013; Li et al. 2018). The neutrinos move at (very near) the speed of light, involve ~ 0.1 to ~ 0.3 solar masses equivalent, and are generically emitted aspherically (see, e.g., Tamborra et al. 2013; Vartanyan et al. 2019a; Walk et al. 2019). The shells of outgoing neutrinos constitute timechanging quadrupoles that source gravitational radiation at frequencies of \sim 0.1–10 Hz (Burrows & Hayes 1996; Müller & Janka 1997; Müller et al. 2012). The high bulk mass-energy and speed of the neutrinos result in their almost complete domination over the matter component for low-frequency gravitational waves in the GW spectrum of CCSNe. While the high-frequency component might boast a product of distance and metric strain (h_+D) of a few centimeters, the neutrino component at those low frequencies is \sim 10–100 cm. However, due to the much lower frequencies and the squared frequency dependence, the energy in this component is much smaller (~a few $\times 10^{-12} M_{\odot}c^2$) than found from the fundamental f-mode signal due to PNS oscillation (Radice et al. 2019). Nevertheless, the neutrino part of the CCSNe GW signature at frequencies of 0.1-10 Hz could be detected by a variety of proposed space- and ground-based GW interferometers (Punturo et al. 2010; Yagi & Seto 2011; Aasi et al. 2015; Sato et al. 2017; Arca Sedda et al. 2019; Maggiore et al. 2020). Stamped on these GW data would be information on the asymmetry of matter and neutrino emissions and characteristic timescales of

explosion and neutron star formation (Braginskii & Thorne 1987; Burrows & Hayes 1996; Müller et al. 2012; Vartanyan et al. 2019a). Hence, the low-frequency channels complement those at higher frequencies to provide a richer picture of supernova dynamics. This would complement the science gleaned from the direct neutrino emissions themselves. In fact, the GW data across the full GW spectral range provides added value—joint GW/neutrino analysis would yield returns that are greater than the sum of the individual parts.

Simulation studies over the last decade have explored the contribution of matter motions, from convective structure to large-scale instabilities such as the SASI (Foglizzo 2002; Blondin & Shaw 2007; Foglizzo et al. 2012), to the development of GWs in 2D and 3D simulations and their subsequent detection (Andresen et al. 2017, 2019; Morozova et al. 2018; Powell & Müller 2019, 2020; Radice et al. 2019; Vartanyan et al. 2019a). Studies have also explored information to be gleaned from detections of neutrino signals with upcoming detectors, such as DUNE and HyperKamiokande (Wallace et al. 2016; Kuroda et al. 2017; Seadrow et al. 2018; Müller 2019b; Vartanyan et al. 2019a). This progress has paralleled growth in detailed multidimensional simulations of CCSNe, many producing robust explosions (Roberts et al. 2016; Müller et al. 2017; O'Connor & Couch 2018; Ott et al. 2018; Radice et al. 2018; Summa et al. 2018; Vartanyan et al. 2018, 2019b; Burrows et al. 2019, 2020; Nagakura et al. 2019; Yoshida et al. 2019; Kuroda et al. 2020).

Less effort, however, has been dedicated to gravitational waveforms from neutrino memory (Burrows & Hayes 1996; Kotake et al. 2007, 2009a; Müller et al. 2012, 2013). Moreover, such studies have either been 2D simulations, or 3D with parameterized neutrino heating. The contribution to GWs from neutrino anisotropies have not been recently studied despite the fact that GWs from CCSNe provide promising candidates for third generation gravitational-wave detectors (Arca Sedda et al. 2019; Srivastava et al. 2019; Cavagliá et al. 2020; Schmitz 2020).

Here, we explore GW signatures from neutrino anisotropies for 13 progenitors from 9 to 60 M_{\odot} , all evolved in 3D with our code FORNAX (Skinner et al. 2019). These models were described in Burrows et al. (2019, 2020). The paper is outlined as follows: in Section 2, we summarize the numerical setup of our simulations and introduce the mathematical framework for studying gravitational waveforms from neutrino anisotropies. In Section 3, we describe our results and explore GWs from neutrino anisotropies as probes of turbulent CCSNe dynamics. We discuss the frequency dependence of the GW signal and the resulting prospects for future detection. We present our conclusions in Section 4.

2. Numerical Setup

FORNAX (Skinner et al. 2019) is a multidimensional, multigroup radiation hydrodynamics code originally constructed to study CCSNe. It features an M1 solver for neutrino transport with detailed neutrino microphysics and a monopole approximation to general relativity (Marek & Janka 2009). In this paper, we study 13 stellar progenitors in 3D, with zero age main sequence masses of 9, 10, 12, 13, 14, 15, 16, 17, 18, 19, 20, 25, and $60~M_{\odot}$ models. All models are initially collapsed in 1D through 10 ms after bounce, and then mapped to three dimensions. For all progenitors except the $25~M_{\odot}$ models, we use Sukhbold et al. (2016). The $25~M_{\odot}$ progenitor is from

Sukhbold et al. (2018). The models and setup here are identical to those discussed in Burrows et al. (2020) and Vartanyan et al. (2019a). We note that all models except the 13, 14, and 15 M_{\odot} progenitors explode (Burrows et al. 2020). Additionally, we note the FORNAX treats three species of neutrinos: electron neutrinos (ν_e), electron antineutrinos ($\bar{\nu}_e$), and μ,τ neutrinos and their antiparticles bundled together as heavy-neutrinos, " ν_{μ} ."

To calculate GWs from neutrino asymmetries, we follow the prescription of Müller et al. (2012). We include angle-dependence of the observer through the viewing angles $\alpha \in [-\pi, \pi]$ and $\beta \in [0, \pi]$. The time-dependent neutrino emission anisotropy parameter for each polarization is defined as

$$\alpha_{S}(t, \alpha, \beta) = \frac{1}{\Lambda(t)} \int_{4\pi} d\Omega' W_{S}(\Omega', \alpha, \beta) \frac{d\Lambda}{d\Omega'}(\Omega', t), \quad (1)$$

where the subscript $S \in \{+, \times\}$ and the GW strain from neutrinos is defined as

$$h_S(t, \alpha, \beta) = \frac{2G}{c^4 D} \int_0^t dt' \, \Lambda(t') \alpha_S(t', \alpha, \beta), \tag{2}$$

where Λ (t) is the angle-integrated neutrino luminosity as a function of time, D is the distance to the source, Ω' is the angular differential in the coordinate frame of the source, and $W_S(\Omega', \alpha, \beta)$ is the geometric weight for the anisotropy parameter given by

$$W_{\rm S} = \frac{D_{\rm S}(\theta', \, \phi', \, \alpha, \, \beta)}{N(\theta', \, \phi', \, \alpha, \, \beta)},\tag{3}$$

where

$$D_{+} = [1 + (\cos(\phi')\cos(\alpha) + \sin(\phi')\sin(\alpha))\sin(\theta')\sin(\beta) + \cos(\theta')\cos(\beta)]\{[(\cos(\phi')\cos(\alpha) + \sin(\phi')\sin(\alpha)) + \sin(\theta')\cos(\beta) - \cos(\theta')\sin(\beta)]^{2} - \sin^{2}(\theta')(\sin(\phi')\cos(\alpha) - \cos(\phi')\sin(\alpha)^{2}\}$$
(4a)

 $D_{\times} = [1 + (\cos(\phi')\cos(\alpha) + \sin(\phi')\sin(\alpha))\sin(\theta')\sin(\beta) + \cos(\theta')\cos(\beta)] 2 [(\cos(\phi')\cos(\alpha) + \sin(\phi')\sin(\alpha)) \sin(\theta')\cos(\beta) - \cos(\theta')\sin(\beta)]\sin(\theta')(\sin(\phi')\cos(\alpha) - \cos(\phi')\sin(\alpha)^{2}$ (4b)

$$N = [(\cos(\phi')\cos(\alpha) + \sin(\phi')\sin(\alpha))\sin(\theta')\cos(\beta) - \cos(\theta')\sin(\beta)]^2 + \sin^2(\theta')(\sin(\phi')\cos(\alpha) - \cos(\phi')\sin(\alpha)^2.$$
(4c)

3. Results and Discussion

In Figure 1, we plot on the left-hand side the neutrino luminosity (equivalent to $\Lambda(t)$ for each neutrino species in Equations (1)–(2)) as a function of time for all 3D models considered here for all three neutrino species. Lower mass models, such as the $9\,M_\odot$ model, in particular, typically have lower neutrino luminosities and accretion rates. Absent explosion, the 13, 14, and $15\,M_\odot$ models accrete for longer and evince higher neutrino luminosities at later times. The development of the spiral SASI (Blondin et al. 2003; Blondin 2005; Blondin & Shaw 2007; Kuroda et al. 2016) is evident for these nonexploding models through the quasi-

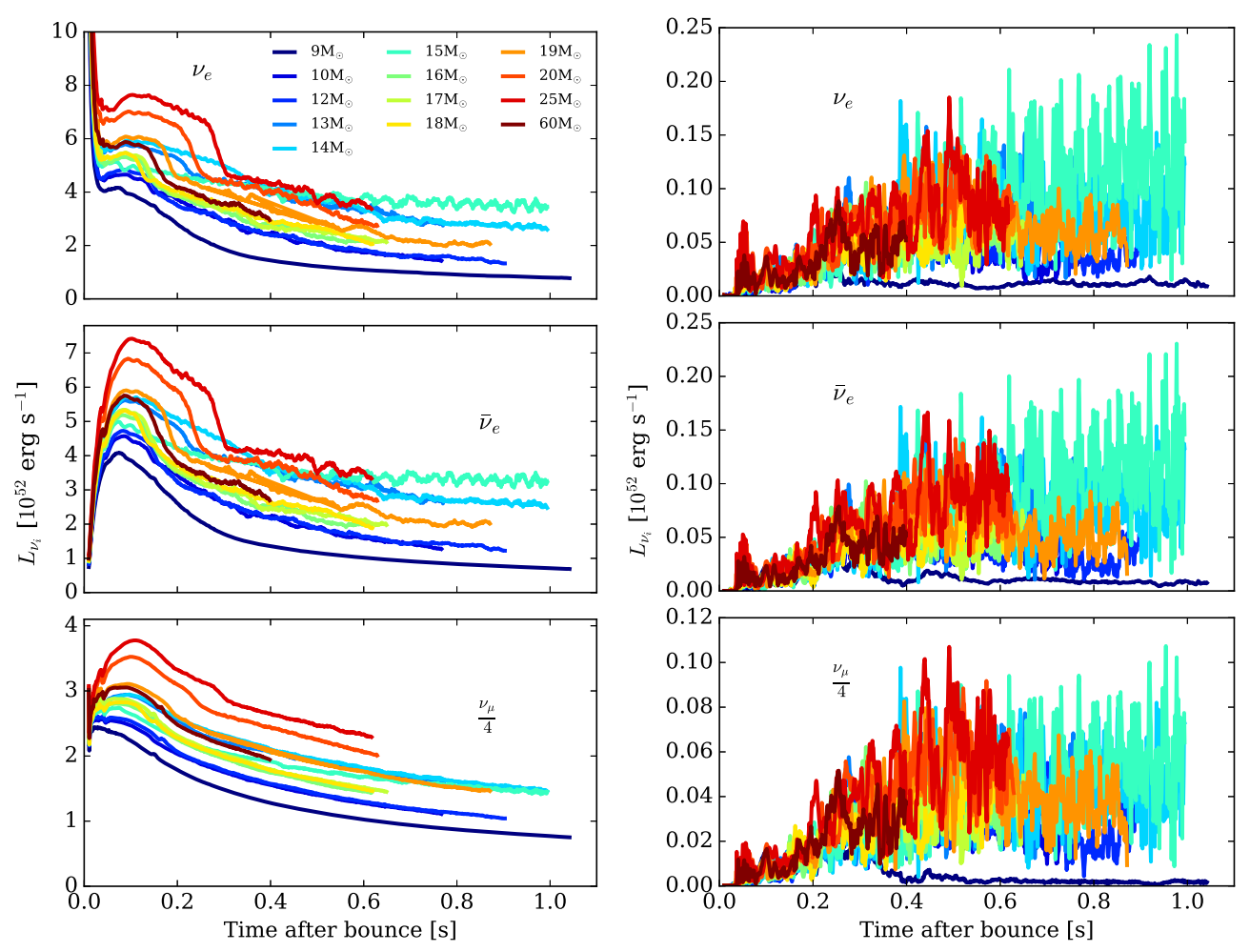


Figure 1. Left: luminosity (in 10^{52} erg s⁻¹) as a function of time after bounce (in seconds) at 250 km, and right: the quadrupole components of the luminosity (in 10^{52} erg s⁻¹) as a function of time after bounce (s) for all three neutrino species. The higher luminosities for the electron neutrinos and antineutrinos for the 13, 14, and $15 M_{\odot}$ progenitors result from sustained accretion for these nonexploding models. The spiral SASI is most evident for the $15 M_{\odot}$ progenitor, which shows periodic oscillations in the neutrino luminosities after \sim 500 ms. The nonexploding models also show large quadrupolar components at later times. However, this does not always yield a higher neutrino gravitational signal. See the text for a discussion.

periodic oscillations after ~500 ms in their neutrino luminosities, and is most visible for the electron neutrinos (ν_e) and antineutrinos $(\bar{\nu}_e)$. We note that we see only the spiral SASI in the nonexploding models. The smaller shock stagnation radii inherently manifest in nonexploding models favor faster advective-acoustic timescales (Foglizzo 2002) that efficiently amplify SASI growth (see Scheck et al. 2008). Recent 3D simulations confirm this for nonexploding, or delayed-exploding, models (Kuroda et al. 2016, 2017; Roberts et al. 2016; Ott et al. 2018; Glas et al. 2019; Vartanyan et al. 2019a, 2019b; Burrows et al. 2020). As indicated in Burrows et al. (2018, 2020) and Vartanyan et al. (2018, 2019b), the majority of our models explode within the first 300 milliseconds, precluding the development of a SASI. Prompt explosion is in large part due to the detailed microphysics of the simulation namely the inclusion of the axial-vector many-body correction to the neutrino-nucleon scattering rates—and to the intrinsic density profile of the progenitors. Generally, we find that models with sharper silicon/oxygen interfaces produce earlier explosion owing to a favorable combination of a sustained neutrino luminosity and a drop in the accreta ram pressure. We also emphasize that the nature of explosion in these models is not absolute—some models seem more explodable than others,

but changes to the evolution physics, progenitor structure, or resolution could alter this conclusion.

In the right-hand side of Figure 1, we plot the quadrupolar neutrino luminosity as a function of time for all 3D models and for all three neutrino species. We use the approach outlined in Burrows et al. (2012; see also Vartanyan et al. 2019a) to decompose the luminosity $L_{\nu}(\theta, \phi)$ into spherical harmonic components with coefficients:

$$a_{lm} = \frac{(-1)^{|m|}}{\sqrt{4\pi(2l+1)}} \oint L_{\nu}(\theta,\phi) Y_l^m(\theta,\phi) d\Omega, \tag{5}$$

normalized such that $a_{00}=a_0=\langle L_\nu\rangle$ (the average neutrino luminosity). $a_{11},\ a_{1-1}$, and a_{10} correspond to the average Cartesian coordinates of the shock surface dipole $\langle x_s\rangle, \langle y_s\rangle$, and $\langle z_s\rangle$, respectively. The orthonormal harmonic basis functions are given by

$$Y_{l}^{m}(\theta, \phi) = \begin{cases} \sqrt{2} N_{l}^{m} P_{l}^{m}(\cos \theta) \cos m\phi & m > 0, \\ N_{l}^{0} P_{l}^{0}(\cos \theta) & m = 0, \\ \sqrt{2} N_{l}^{|m|} P_{l}^{|m|}(\cos \theta) \sin|m|\phi & m < 0, \end{cases}$$
(6)

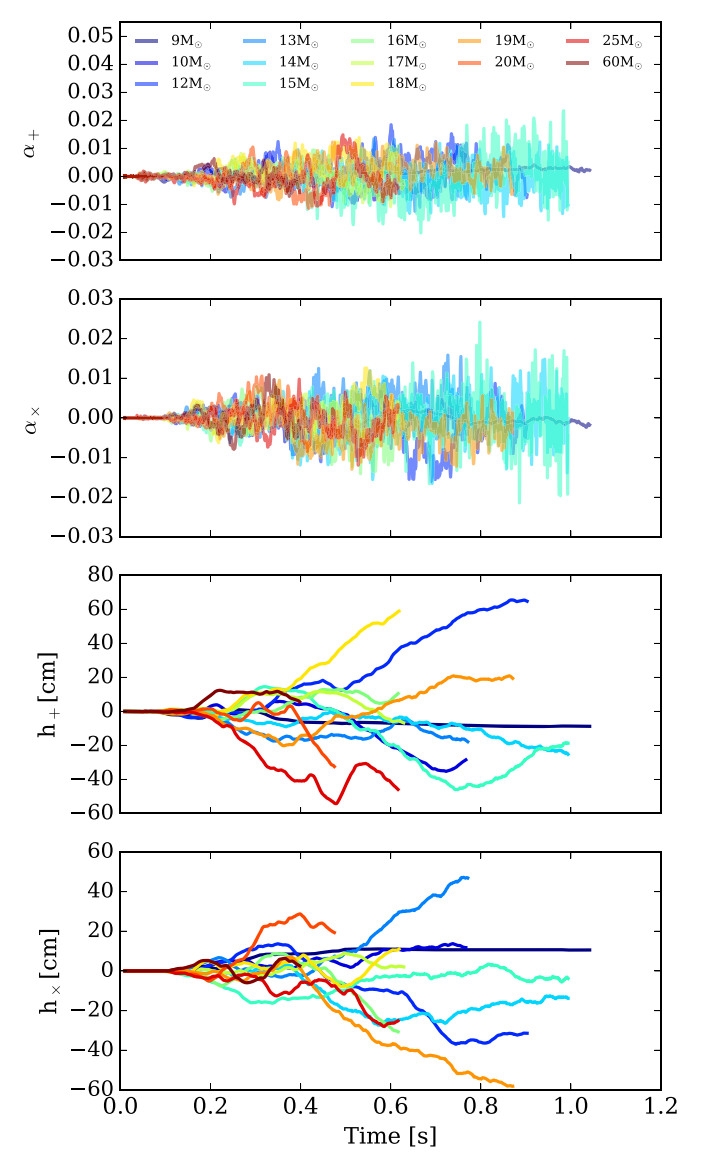


Figure 2. We show the neutrino anisotropy parameters for the electron-type neutrinos for both polarizations (top two panels), and the GW strain summed over all species of neutrinos for both polarizations (bottom panels). The values are measured along the negative *x*-axis.

where

$$N_l^m = \sqrt{\frac{2l+1}{4\pi} \frac{(l-m)!}{(l+m)!}},$$
(7)

 $P_l^m(\cos \theta)$ are the associated Legendre polynomials, and θ and ϕ are the spherical coordinate angles.

We define the quadrupolar component of the neutrino luminosity as the following norm,

$$L_{\nu,\ell} = \frac{\sqrt{\sum_{m=-\ell}^{\ell} a_{\ell m}^2}}{a_{00}},\tag{8}$$

where we take $\ell = 2$.

The quadrupolar neutrino luminosity is at most a few percent of the total neutrino luminosity. Note that the exploding models peak at $\sim\!\!0.5$ s after bounce, after which the nonexploding models develop the largest quadrupolar components due to the

onset of the spiral SASI. The weakly exploding $9 M \odot$ progenitor shows the smallest asymmetry.

In Figure 2, we show the geometric anisotropy parameter along the negative x-axis for the electron-type neutrinos for the + polarization (top panel) and the ×polarization (second panel from the top). The neutrino anisotropies can get as strong as several percent, in accordance with the quadrupolar component of the neutrino luminosity. This is a factor of several higher than for the 3D simulations from Müller et al. (2012). Although the "heavy"-neutrinos show similar or slightly smaller geometric anisotropy parameters, they dominate the neutrino luminosity and hence the GW strain, plotted for + and \times polarizations in the bottom two panels, respectively, summed over all neutrino species. Note that we see a similar hierarchy between neutrino species and their spatial variation here as in Vartanyan et al. (2019a), using different formalisms for the neutrino anisotropy. The anisotropy parameters for the nonexploding models are largest for all species at late times, after \sim 500 ms, corresponding to the development of the spiral SASI. However, a larger anisotropy parameter does not directly translate into higher strains, as visible in the bottom two panels of Figure 2, due to additive cancellation when integrating Equation (2) over time.

The neutrino gravitational strain is approximately two orders of magnitude larger than the matter GW strain and shows secular growth with time. The neutrino strain is significantly different from the matter component (Morozova et al. 2018; Radice et al. 2019)—it features weaker time variations and larger amplitudes, with more monotonic behavior with time. This reflects the fundamental differences of their origins. GWs from matter involve $\sim 0.1~M_{\odot}$ with convective velocities of \sim 1000 km s⁻¹ on convective timescales of milliseconds (Vartanyan et al. 2019b; Nagakura et al. 2020). On the other hand, neutrino luminosity contributions involve relativistic velocities and significant energy losses from the PNS. The memory effect (Braginskii & Thorne 1987) from neutrinos, indicated as the integral over time in Equation (2), smooths over small timescale variations and allows cumulative growth of the neutrino strain.

We comment on the $9\,M\odot$ progenitor, which explodes early and more isotropically than later exploding models, such as the 19 and $60\,M\odot$ progenitors (Burrows et al. 2020). Early, spherical explosion and the cessation of accretion was associated with a weaker GW signal from matter motions. Radice et al. (2019) emphasized that accretion, and not solely PNS convection, was responsible for driving matter GWs. The $9\,M_\odot$ is a good example of this distinction—the PNS is convective at late times (Nagakura et al. 2020), but accretion has ended. Here, we further associate the cessation of accretion with a weak GW signal from neutrino anisotropies. The $9\,M_\odot$ progenitor has both small anisotropy parameters in Figure 2 and small strains.

Note that all models take $\sim 100-200$ ms for the neutrino anisotropy to manifest and result in a nonzero strain. This corresponds to the timescale for turbulence to develop and for the supernova shock to break spherical symmetry. Note that, unlike the matter component of GWs, neutrinos do not show a prompt-convection burst shortly after bounce. However, like the matter component, there is a hiatus of $\sim 100-200$ ms.

Lastly, we see large excursions from monotonic growth of the strain for several models due to the delay until fully developed turbulence arises. Neglecting azimuthal-variations for the sake of simplicity, we can understand the strain evolution through the evolving geometry of the explosion. We take the + polarization for an observer along the negative xaxis, where positive strains correspond to axial motions, and negative strains to equatorial motions (see also Kotake et al. 2009a for a 2D analog along the equatorial plane). The 25 M_{\odot} progenitor has a large negative strain until ~400 ms postbounce, when the model explodes. We see a corresponding positive bump in the α_{+} in the top panel of Figure 2, and a positive bump in h_{+} , which corresponds to the deformation of the shock as it begins to expand. Additionally, the nonexploding progenitors maintain small strains until ~500 ms postbounce, when the spiral SASI develops. The 15 M_{\odot} progenitor (in cyan) develops a large negative h_+ , corresponding to an equatorial spiral SASI. Within a few hundred milliseconds, the strain becomes less negative as the spiral SASI precesses. We emphasize that this conclusion depends on the observer direction.

We illustrate the three-dimensional GW emission from neutrinos for both polarizations in Figure 3 at 153 and 249 ms post-bounce for the $19 M_{\odot}$ progenitor as a function of viewing angle. Here, colors are degenerate with the contours: hotter colors and convex surfaces indicate larger positive values of the strain, and cooler colors and concave surfaces indicate larger negative values of the strain. To emphasize the dependence on viewing angle, we illustrate in Figure 4 the same map of the GW-emission rotated by 180° in azimuth. The prompt rise in the GW energy from matter contributions at ~ 50 ms corresponds to prompt convection following neutrino breakout. The energy growth then stalls for ~ 100 ms, before reaching values as high as $\sim 10^{46}$ erg, and less than $\sim 10^{44}$ erg for the lowest energy, for the $9 M_{\odot}$ model. The stall time for the GW energy to ramp up indicates the timescale for turbulence to develop in the CCSN. This timescale for matter is not dissimilar for that from neutrinos: ~100 ms. On the other hand, the energy in GWs from neutrinos can be as high as 10^{43} erg, and as low as 10^{41} erg, again for the $9 M_{\odot}$ model. We note that these values are still increasing at the end of our simulation, as is the explosion energy, and longer 3D simulations are required to capture the asymptotic behavior. Additionally, nonexploding models have powerful GW signatures in both neutrinos and matter at late times that are associated with the development of the spiral SASI, which modulates the infalling accretion to source GWs.

In Figure 5, we show the GW energies from neutrino anisotropies on the left for all our models, and from matter on the right. Note that, although neutrinos dominate the gravitational strain by as much as two orders of magnitude, matter dominates the GW energy by as much as three orders of magnitude. This is simply because GW energy scales as the square of the product of the strain and the frequency, and the neutrino component resides at much lower frequencies (see Figure 7), indicative of its secular evolution and the memory effect.

3.1. Frequency Dependence

In Figure 6, we provide Fourier transforms of the neutrino luminosity for all three species, subtracting out the mean over a 30 ms running average, as a function of frequency (in Hz) for the $14\,M_\odot$ progenitor (left) and the $19\,M_\odot$ progenitor (right). All neutrino species show similar frequency behavior with a weak hierarchy in power in the order ν_e , $\bar{\nu}_e$, and ν_μ , similar to

the results in Vartanyan et al. (2019a). We see significant power at low frequencies corresponding to the longer secular timescales of order one second. The $14\,M_\odot$ progenitor, which does not explode, shows a significant bump in power at $\sim 150\,$ Hz, corresponding to the development of the spiral SASI. Such a low-power component, between 100 and 200 Hz, has been well-identified with the SASI, which has modulation timescales of $\sim O(10\,$ ms) (Blondin & Shaw 2007; Kotake et al. 2009b; Kuroda et al. 2016, 2017; Andresen et al. 2017). The exploding $19\,M_\odot$ progenitor has no SASI development.

In Figure 7, we provide GW energy spectrograms (in B $\rm Hz^{-1}$) from neutrino anisotropies of the nonexploding $14\,M_\odot$ progenitor (left), and the exploding $60\,M_\odot$ progenitor (right) as a function of time after bounce (s) and frequency (Hz). To compute the spectrograms, we apply a Hann window function to the GW energy spectra and take a short time Fourier transform with a window size of 40 ms. Our sampling frequency is $1000\,\rm Hz$. Note that most of the power lies below $50\,\rm Hz$, with less power at higher frequencies. The spiral SASI in nonexploding models, like the $14\,M_\odot$ progenitor, contributes to this higher frequency power.

3.2. Detection Prospects

In Figure 8, we plot the GW amplitude spectral density at 10 kiloparsecs for all models studied in 3D, indicating both the neutrino component (stars) and matter component (circles) and compare with the sensitivity of current and proposed GW missions. Although we show the matter and neutrino components separately, in reality they combine into the net GW strain. However, as illustrated, they dominate at different frequency ranges. Above $\sim\!100$ Hz, the matter component dominates, peaking at $1000\,\mathrm{Hz}$, corresponding to convective timescales. The neutrino component dominates below $100\,\mathrm{Hz}$ and plateaus below a few tens of hertz.

We overplot the sensitivity curves for three detectors: Advanced-LIGO (Zero-Det High-P design), the Einstein Telescope (design D), and DECIGO. Advanced-LIGO will be able to resolve GWs for a galactic CCSN from ~ten to a few thousand hertz (Aasi et al. 2015). The Einstein Telescope (Punturo et al. 2010; Maggiore et al. 2020), a ground-based detector with a triangle distribution of arms with baselines of 10 km (as opposed to four for aLIGO) will provide improved sensitivity down to 1 Hz, capable of detecting even lower mass progenitors with weaker GW signals. DECIGO is a spacebased heliocentric mission in the style of LISA, but with much smaller arms (1000 km) and much improved sensitivity at decihertz frequencies owing to its Fabry-Perot interferometers. We note that the high-frequency cutoff for our neutrino and matter components is simply the Nyquist frequency due to our data sampling. The lower frequency cutoff for the neutrino component is due to the length of our simulations—our 3D models were carried out at most to ~ 1 s after bounce. Longer simulations will populate this lower frequency detection space. Third generation GW detectors will provide broadband coverage of galactic supernovae sensitive to both matter and neutrino asymmetries.

4. Conclusions

Recent proliferation in 3D simulation capabilities of CCSNe in the first second after bounce have additionally provided new insights into the information contained in the GWs sourced by

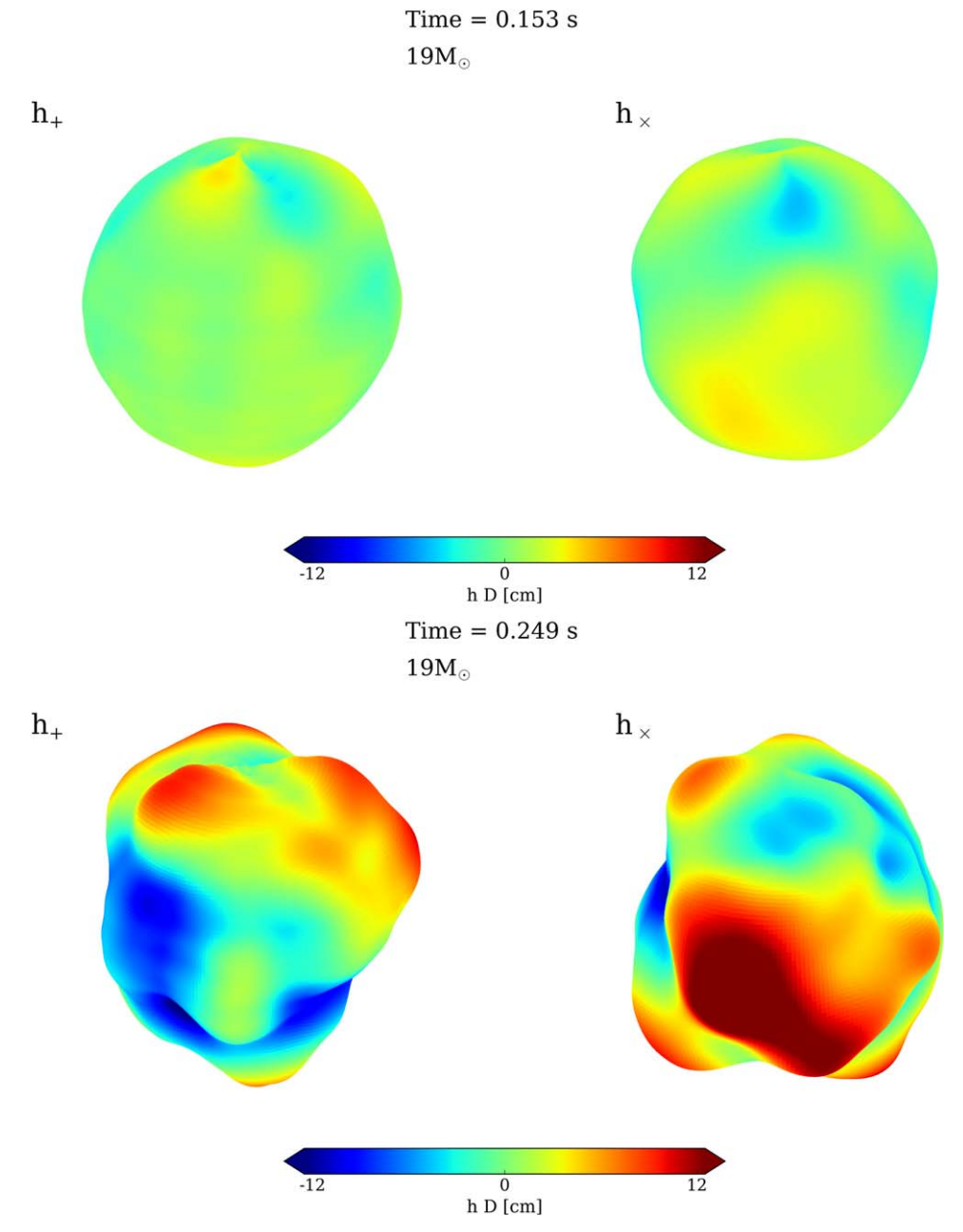


Figure 3. Three-dimensional map illustrating the gravitational-wave strain h (multiplied by distance D) generated by neutrino emission anisotropies 253 ms after bounce, assuming a stellar progenitor with mass $19 M_{\odot}$. The signal is shown for both h_{+} (left) and h_{\times} (right) polarization, and as a function of the viewing angle. Hotter colors (yellow to red; convex surfaces), indicate positive strains, whereas cooler colors (blue to yellow; concave surfaces) indicate negative strains.

matter and in neutrino signatures. However, study of GWs sourced by neutrino asymmetries has lagged. Axisymmetric 2D studies overestimate the development of axial instabilities and of the strains in general. Additionally, simplified 3D studies, often with parameterized neutrino heating, are insufficient to study the development of neutrino asymmetries critical to understanding neutrino gravitational waveforms. Thus, 3D simulations with detailed neutrino transport are essential to study with fidelity the neutrino waveforms for CCSNe. We presented here a study of the latter, which complements matter GWs and provides new insights. The neutrino component is fundamentally different from the matter component, involving variations of relativistic radiation on secular timescales. As a result, neutrino asymmetries of only a few percent can culminate in large gravitational strains.

Despite great advances in simulation studies of CCSNe this last decade, there is still much to accomplish. In particular, the GW emissions depend on the implementation of general relativity in a supernovae code, and in FORNAX we rely on a monopole approximation to relativistic gravity. In addition, improvements to the radiation transport algorithm and the neutrino microphysics will alter the neutrino heating profile of CCSNe. Moreover, higher resolution studies (e.g., Nagakura et al. 2019) may be required to capture the development of turbulence down to small scales and could result in modifications to the explosion and geometry. Lastly, longer-duration simulations, out to at least several seconds, are essential to understand the late-time asymptotic behavior of CCSNe.

In this paper, we looked at a sequence of progenitors from 9 to 60 M_{\odot} evolved in 3D. Compared to the matter waveforms,

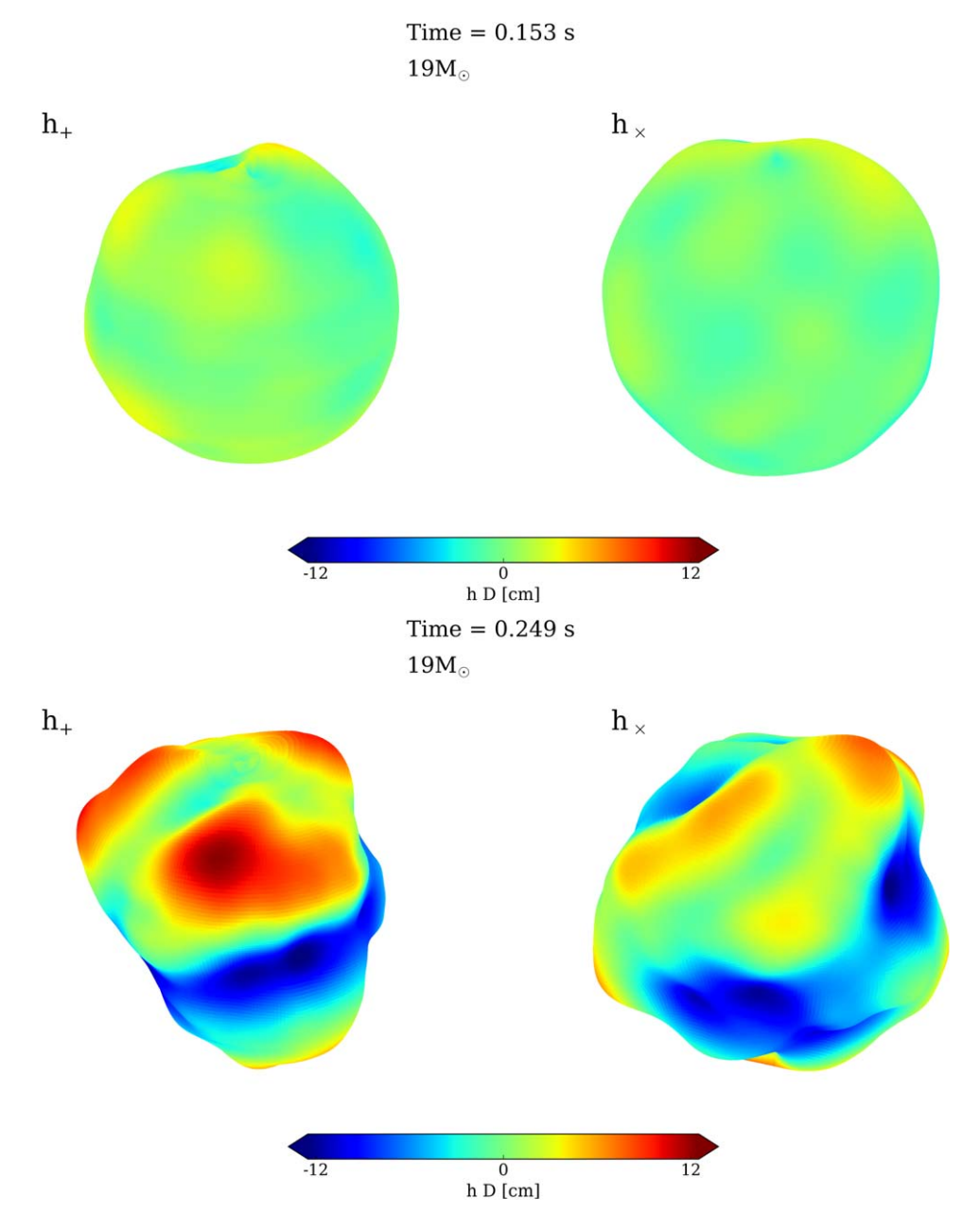


Figure 4. Same as Figure 3, but now with the viewing angle rotated by 180° along the azimuth.

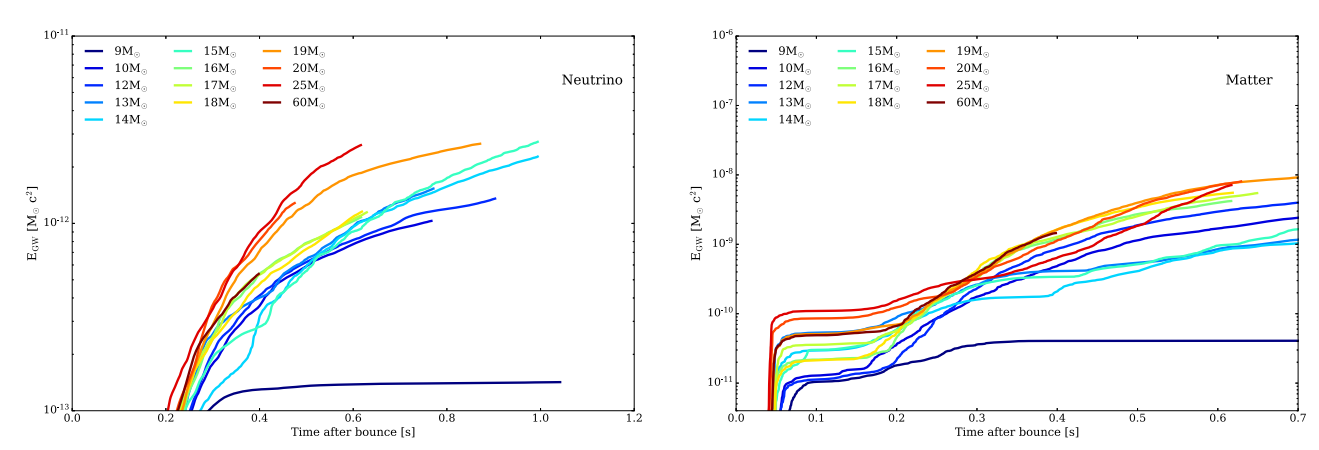


Figure 5. Here, we compare the contribution to the GW energy (in $M_{\odot}c^2$) from neutrino (left) and matter (right) quadrupolar asymmetries for the various models studied in 3D as a function of time after bounce (in seconds). Note the vastly different scales on the y-axis. Neutrino contributions to the GW energies are more than three orders of magnitude smaller than those due to matter motions.

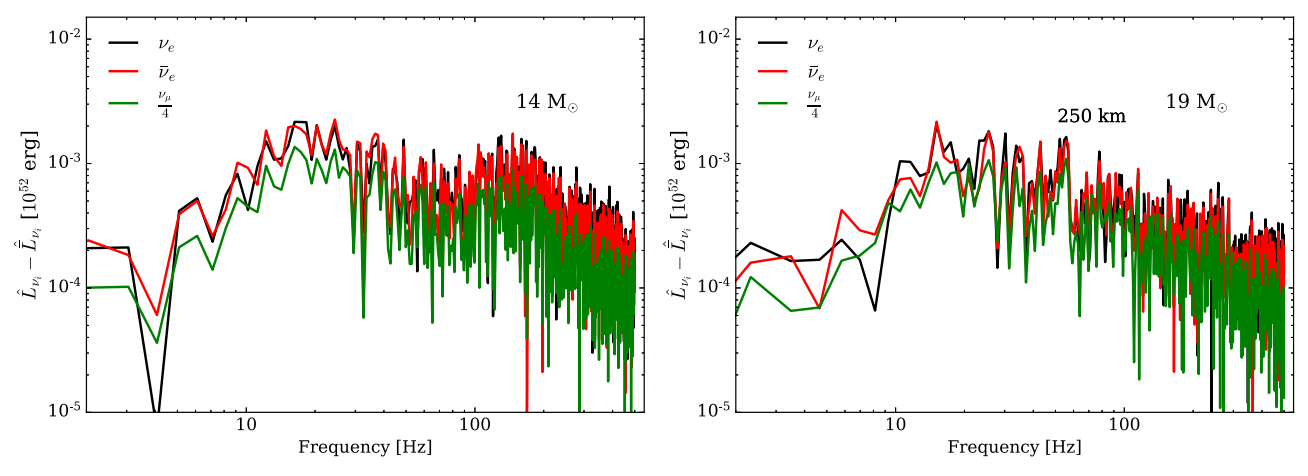


Figure 6. Fourier transform of the neutrino luminosity for all three species, subtracting out the mean over a 30 ms running average, as a function of frequency (Hz). We see significant power at low frequencies corresponding to the longer secular timescales of the order of 1 s. The $14 M_{\odot}$ progenitor (left), which does not explode, shows a significant bump in power at \sim 150 Hz, corresponding to the development of the spiral SASI. The $19 M_{\odot}$ progenitor (right), which does explode, is absent the SASI and the corresponding neutrino signature. Both models also show a slight bump at \sim 300 Hz, corresponding to the timescales of small-scale convection in the PNS core.

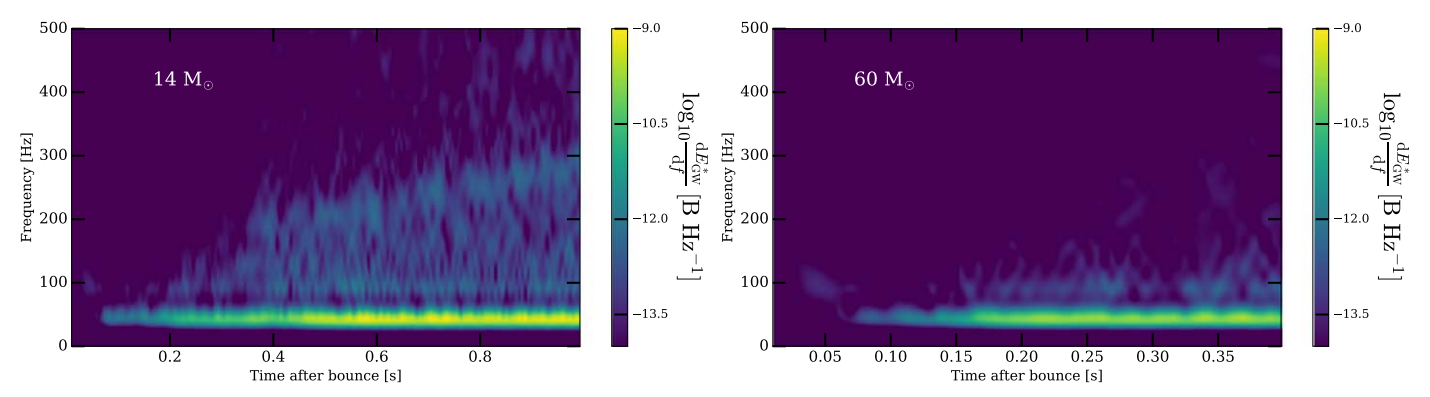


Figure 7. GW energy spectrogram (in B ${\rm Hz}^{-1}$) from neutrino anisotropies of the nonexploding $14\,M_\odot$ progenitor (left), and the exploding $60\,M_\odot$ progenitor (right) as a function of time after bounce (s) and frequency (Hz). Note that most power lies below 50 Hz, with less power at higher frequencies. The spiral SASI in nonexploding models, like the $14\,M_\odot$ progenitor, contributes to this power.

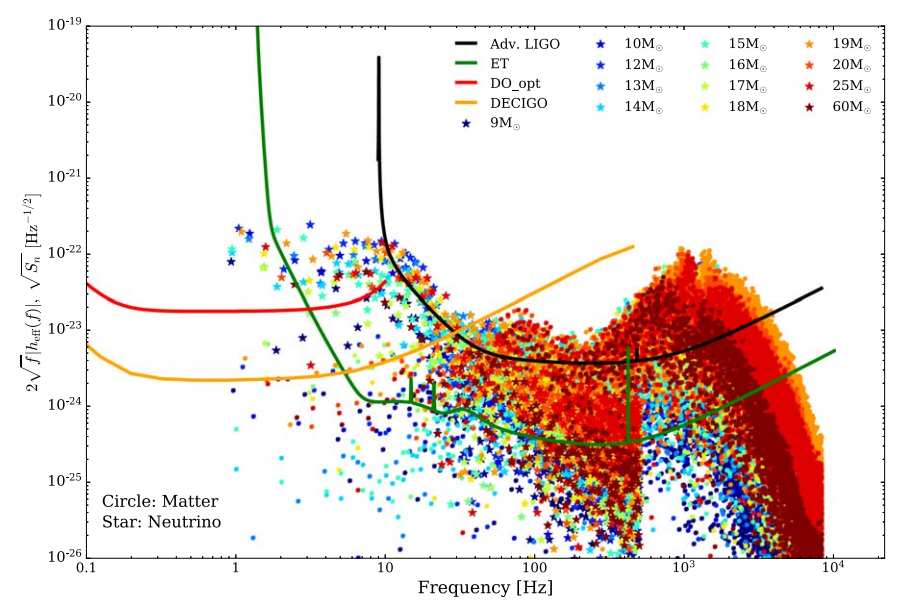


Figure 8. We plot the amplitude spectral density at 10 kpc (in $\text{Hz}^{-1/2}$) spanning $\sim 1-10,000 \text{ Hz}$ for all the models studied in 3D. The neutrino component (stars) dominates from sub-Hz to several hundred Hz, whereas the matter component (circles) dominates above several hundred Hz. We also overplot the sensitivity curves for current and upcoming GW detectors. Many detectors, including aLIGO, DECIGO, and ET, will be able to detect GWs from a galactic CCSN event. DO_opt indicates an optimal decihertz observatory between 2035 and 2050 (Arca Sedda et al. 2019) lying between LISA and ground-based detectors in frequency band designed to detect intermediate mass black hole binaries, a few $\sim 10 \text{ s}$ to a few $\sim 100 \text{ s}$ M_{\odot} , with the added value of detection capabilities for galactic CCSNe.

we find that the neutrino waveforms can be up to two orders of magnitude larger in strain. Additionally, the neutrino waveform shows much less time variation and quasi-monotonic evolution due to the integral nature of the neutrino memory. However, whereas the matter component dominates at 100–1000 s of Hertz, the neutrino component dominates at a few tens of hertz, and hence, contributes much less to the GW energy. Unlike the matter component, the neutrino contribution to the gravitational waveform does not have a prompt convective signal. However, both matter and neutrino GWs trace the development of turbulence in the first hundreds of milliseconds after bounce.

We find an approximate trend with progenitor mass and neutrino strain strength, which probes the strength of the accretion driving turbulence that manifests the GWs and identifies both small-scale instabilities, like convection, and larger-scale instabilities like the spiral SASI. The $9\,M_\odot$ progenitor, with a weak and short-lived accretion history, shows the smallest neutrino asymmetries and gravitational waveforms. However models, like the $25\,M_\odot$, which sustain longer and more powerful accretion experience larger sustained gravitational strains.

For models that do not explode, namely the 13, 14, and $15\,M_\odot$, we find signatures of the spiral SASI in both the neutrino luminosities and the neutrino gravitational waveforms at $\sim \! 100$ Hz, coincident with the matter gravitational waveform (Vartanyan et al. 2019a). Due to the quadrupolar nature of the strain, its sign and magnitude illustrate the geometry of explosion and indicate, for instance, the development of equatorial or axial deformations in the propagating shock front. Additionally, the strain probes the precession of the spiral SASI for nonexploding models.

Lastly, we find that neutrino GWs can be detectable for galactic events by aLIGO as well as by DECIGO and the Einstein Telescope. Future detections of GWs from galactic CCSNe will explore the development of turbulence, the explosion morphology, the accretion history, and the success or failure of explosion. Additionally, the low-frequency GWs around 1 Hz, will probe the secular evolution of CCSNe, longer after explosion. CCSNe emit neutrinos for many seconds after explosion, and modeling these will require carrying out much longer 3D simulations.

The authors acknowledge fruitful collaborations and discussions with David Radice, Hiroki Nagakura, Daniel Kasen, and Sherwood Richers. D.V. and A.B. acknowledge support from the U.S. Department of Energy Office of Science and the Office of Advanced Scientific Computing Research via the Scientific Discovery through Advanced Computing (SciDAC4) program and Grant DE-SC0018297 (subaward 00009650) and support from the U.S. NSF under grants AST-1714267 and PHY-1804048 (the latter via the Max-Planck/Princeton Center (MPPC) for Plasma Physics). A generous award of computer time was provided by the INCITE program. That research used resources of the Argonne Leadership Computing Facility, which is a DOE Office of Science User Facility supported under Contract DE-AC02-06CH11357. In addition, this overall research project is part of the Blue Waters sustained-petascale computing project, which is supported by the National Science Foundation (awards OCI-0725070 and ACI-1238993) and the state of Illinois. Blue Waters is a joint effort of the University of Illinois at Urbana-Champaign and its National Center for Supercomputing Applications. This general project is also part

of the "Three-Dimensional Simulations of Core-Collapse Supernovae" PRAC allocation support by the National Science Foundation (under award #OAC-1809073). Moreover, we acknowledge access under the local award #TG-AST170045 to the resource Stampede2 in the Extreme Science and Engineering Discovery Environment (XSEDE), which is supported by National Science Foundation grant number ACI-1548562. Finally, the authors employed computational resources provided by the TIGRESS high performance computer center at Princeton University, which is jointly supported by the Princeton Institute for Computational Science and Engineering (PICSciE) and the Princeton University Office of Information Technology, and acknowledge our continuing allocation at the National Energy Research Scientific Computing Center (NERSC), which is supported by the Office of Science of the US Department of Energy (DOE) under contract DE-AC03-76SF00098.

Software: FORNAX (Skinner et al. 2019).

ORCID iDs

David Vartanyan https://orcid.org/0000-0003-1938-9282 Adam Burrows https://orcid.org/0000-0002-3099-5024

References

```
Aasi, J., Abbott, B. P., Abbott, R., et al. 2015, CQGra, 32, 074001
Andresen, H., Müller, B., Müller, E., & Janka, H. T. 2017, MNRAS, 468, 2032
Andresen, H., Müller, E., Janka, H. T., et al. 2019, MNRAS, 486, 2238
Arca Sedda, M., Berry, C. P. L., Jani, K., et al. 2019, arXiv:1908.11375
Blondin, J. M. 2005, JPhCS, 16, 370
Blondin, J. M., Mezzacappa, A., & DeMarino, C. 2003, ApJ, 584, 971
Blondin, J. M., & Shaw, S. 2007, ApJ, 656, 366
Braginskii, V. B., & Thorne, K. S. 1987, Natur, 327, 123
Burrows, A., Dolence, J. C., & Murphy, J. W. 2012, ApJ, 759, 5
Burrows, A., & Hayes, J. 1996, PhRvL, 76, 352
Burrows, A., Radice, D., & Vartanyan, D. 2019, MNRAS, 485, 3153
Burrows, A., Radice, D., Vartanyan, D., et al. 2020, MNRAS, 491, 2715
Burrows, A., Vartanyan, D., Dolence, J. C., Skinner, M. A., & Radice, D.
          SSRv, 214, 33
Cavagliá, M., Gaudio, S., Hansen, T., et al. 2020, Mach. Learn.: Sci. Technol.,
   1, 015005
Christodoulou, D. 1991, PhRvL, 67, 1486
Couch, S. M., Warren, M. L., & O'Connor, E. P. 2020, ApJ, 890, 127
Epstein, R. 1978, ApJ, 223, 1037
Foglizzo, T. 2002, A&A, 392, 353
Foglizzo, T., Masset, F., Guilet, J., & Durand, G. 2012, PhRvL, 108, 051103
Glas, R., Janka, H. T., Melson, T., Stockinger, G., & Just, O. 2019, ApJ,
Holgado, A. M., & Ricker, P. M. 2019, MNRAS, 490, 5560
Kotake, K. 2010, JPhCS, 229, 012011
Kotake, K., Iwakami, W., Ohnishi, N., & Yamada, S. 2009a, ApJ, 704, 951
Kotake, K., Iwakami, W., Ohnishi, N., & Yamada, S. 2009b, ApJL, 697, L133
Kotake, K., Iwakami-Nakano, W., & Ohnishi, N. 2011, ApJ, 736, 124
Kotake, K., Ohnishi, N., & Yamada, S. 2007, ApJ, 655, 406
Kotake, K., Sato, K., & Takahashi, K. 2006, RPPh, 69, 971
Kuroda, T., Arcones, A., Takiwaki, T., & Kotake, K. 2020, ApJ, 896, 102
Kuroda, T., Kotake, K., Hayama, K., & Takiwaki, T. 2017, ApJ, 851, 62
Kuroda, T., Kotake, K., & Takiwaki, T. 2016, ApJL, 829, L14
Li, J.-T., Fuller, G. M., & Kishimoto, C. T. 2018, PhRvD, 98, 023002
Mabanta, Q. A., Murphy, J. W., & Dolence, J. C. 2019, ApJ, 887, 43
Maggiore, M., Broeck, C. V. D., Bartolo, N., et al. 2020, JCAP, 2020, 050
Marek, A., & Janka, H.-T. 2009, ApJ, 694, 664
Mezzacappa, A., Marronetti, P., Landfield, R. E., et al. 2020, PhRvD, 102,
   023027
Morozova, V., Radice, D., Burrows, A., & Vartanyan, D. 2018, ApJ, 861, 10
Müller, B. 2019a, MNRAS, 487, 5304
Müller, B. 2019b, ARNPS, 69, 253
Müller, B., Janka, H.-T., & Marek, A. 2013, ApJ, 766, 43
Müller, B., Melson, T., Heger, A., & Janka, H.-T. 2017, MNRAS, 472, 491
```

Müller, E., & Janka, H. T. 1997, A&A, 317, 140

```
Müller, E., Janka, H. T., & Wongwathanarat, A. 2012, A&A, 537, A63
Murphy, J. W., Ott, C. D., & Burrows, A. 2009, ApJ, 707, 1173
Nagakura, H., Burrows, A., Radice, D., & Vartanyan, D. 2019, MNRAS,
   490, 4622
Nagakura, H., Burrows, A., Radice, D., & Vartanyan, D. 2020, MNRAS,
   492, 5764
O'Connor, E. P., & Couch, S. M. 2018, ApJ, 865, 81
Ott, C. D., Roberts, L. F., da Silva Schneider, A., et al. 2018, ApJL, 855, L3
Powell, J., & Müller, B. 2019, MNRAS, 487, 1178
Powell, J., & Müller, B. 2020, MNRAS, 494, 4665
Punturo, M., Abernathy, M., Acernese, F., et al. 2010, CQGra, 27, 194002
Radice, D., Abdikamalov, E., Ott, C. D., et al. 2018, JPhG, 45, 053003
Radice, D., Burrows, A., Vartanyan, D., Skinner, M. A., & Dolence, J. C.
   2017, ApJ, 850, 43
Radice, D., Morozova, V., Burrows, A., Vartanyan, D., & Nagakura, H. 2019,
   ApJL, 876, L9
Roberts, L. F., Ott, C. D., Haas, R., et al. 2016, ApJ, 831, 98
Sato, S., Kawamura, S., Ando, M., et al. 2017, JPhCS, 840, 012010
Scheck, L., Janka, H.-Th., Foglizzo, T., & Kifonidis, K. 2008, A&A, 477, 931
Schmitz, K. 2020, arXiv:2002.04615
Seadrow, S., Burrows, A., Vartanyan, D., Radice, D., & Skinner, M. A. 2018,
  MNRAS, 480, 4710
```

Skinner, M. A., Dolence, J. C., Burrows, A., Radice, D., & Vartanyan, D.

2019, ApJS, 241, 7

```
Sotani, H., Kuroda, T., Takiwaki, T., & Kotake, K. 2017, PhRvD, 96, 063005
Srivastava, V., Ballmer, S., Brown, D. A., et al. 2019, PhRvD, 100, 043026
Sukhbold, T., Ertl, T., Woosley, S. E., Brown, J. M., & Janka, H.-T. 2016, ApJ,
  821, 38
Sukhbold, T., Woosley, S. E., & Heger, A. 2018, ApJ, 860, 93
Summa, A., Janka, H.-T., Melson, T., & Marek, A. 2018, ApJ, 852, 28
Tamborra, I., Hanke, F., Müller, B., Janka, H.-T., & Raffelt, G. 2013, PhRvL,
   111, 121104
Thorne, K. S. 1992, PhRvD, 45, 520
Torres-Forné, A., Cerdá-Durán, P., Passamonti, A., & Font, J. A. 2018,
   MNRAS, 474, 5272
Torres-Forné, A., Cerdá-Durán, P., Passamonti, A., Obergaulinger, M., &
  Font, J. A. 2019, MNRAS, 482, 3967
Turner, M. S. 1978, Natur, 274, 565
Vartanyan, D., Burrows, A., & Radice, D. 2019a, MNRAS, 489, 2227
Vartanyan, D., Burrows, A., Radice, D., Skinner, M. A., & Dolence, J. 2018,
   MNRAS, 477, 3091
Vartanyan, D., Burrows, A., Radice, D., Skinner, M. A., & Dolence, J. 2019b,
   MNRAS, 482, 351
Walk, L., Tamborra, I., Janka, H.-T., & Summa, A. 2019, PhRvD, 100, 063018
Wallace, J., Burrows, A., & Dolence, J. C. 2016, ApJ, 817, 182
Yagi, K., & Seto, N. 2011, PhRvD, 83, 044011
```

Yoshida, T., Takiwaki, T., Kotake, K., et al. 2019, ApJ, 881, 16